JACS
JOURNAL OF THE AMERICAN CHEMICAL SOCIETY
Article
pubs.acs.org/JACS

Monodisperse Copper Chalcogenide Nanocrystals: Controllable Synthesis and the Pinning of Plasmonic Resonance Absorption

Feifan Wang,[†,‡] Qi Li,[*,†] Li Lin,[§] Hailin Peng,[§] Zhongfan Liu,[§] and Dongsheng Xu[*,†,‡]

[†]Beijing National Laboratory for Molecular Sciences, State Key Laboratory for Structural Chemistry of Unstable and Stable Species, College of Chemistry and Molecular Engineering, Peking University, Beijing 100871, P. R. China

[‡]Academy for Advanced Interdisciplinary Studies, Peking University, Beijing 100871, P. R. China

[§]Center for Nanochemistry, Beijing Science and Engineering Center for Nanocarbons, Beijing National Laboratory for Molecular Sciences, College of Chemistry and Molecular Engineering, Peking University, Beijing 100871, P. R. China

Supporting Information

ABSTRACT: Controllable synthesis of copper chalcogenide nanocrystals (NCs), including desired geometry, composition and surrounding environment, is of high significance for the modulation of their optoelectronic response and the corresponding applications. Herein, copper nitride nanoparticles have been used as "uncontaminated" copper precursors to synthesize copper chalcogenide NCs with high monodispersity through a one-pot strategy. In this protocol, the sizes and compositions of NCs can be readily controlled by varying the ratio of the precursors. For $Cu_{2-x}S$ NCs with different diameters, the size variations are all smaller than 5.6%. Furthermore, the plasmonic properties of the copper chalcogenide NCs are investigated under a steady state by tuning the plasmonic resonance absorption band to a limiting condition (denoted "pinning" phenomena). It is observed that the pinning frequency increases (from 1.09 to 1.23 eV) with the increment of the NC size (from 5.4 ± 0.3 to 11.1 ± 0.4 nm), explained by introducing surface scattering. Meanwhile, the frequencies of ternary alloyed copper sulfide selenide NCs blue-shift from 0.90 to 1.00 eV with the increase of selenium content from 11% to 66%, which is related to the effective mass of free carriers. Additionally, the plasmonic absorption bands of $Cu_{2-x}S$ NCs encapsulated by two single-layer graphene pin at 1525−1550 nm during the oxidation process, which is influenced by both the dielectric constant and redox potential of the surrounding environment. This study demonstrates the controllable synthesis and precise fundamental plasmonic properties of the copper chalcogenide NCs, ensuring the potential plasmonic-related techniques with high efficiency, accuracy and excellent spatial resolution.

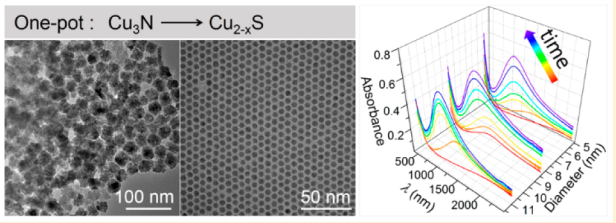

INTRODUCTION

When exerting an incident light on a plasmonic nanostructure, the free carriers are driven to oscillate collectively at a resonant frequency, which is characterized as the localized surface plasmon resonance (LSPR).[1,2] By controlling the fabrication of noble metal nanostructures with a desired size, shape, composition and dielectric environment, one can exquisitely tailor the optical properties of these structures for various applications, ranging from medicine to electronics.[2−7] Recently, plasmonic semiconductor materials are under intense investigation.[8−10] Doped semiconductors usually have lower loss at optical frequencies than the conventional noble metals due to their lower carrier concentration, which endows them the advantage over metals in transformation-optics and metamaterial devices.[8]

Another advantage of the plasmonic semiconductor nanocrystals (NCs) is the tunable optical response from visible to infrared range, because their free carrier density can be tuned over several orders of magnitude. For copper chalcogenide NCs, also called the "self-doped semiconductors", the oxidation tuning of the near-infrared (NIR) plasmonic absorption can be achieved by the ambient oxygen under different temperatures[11−13] or metal salt solutions (e.g., Ce^{4+} cations).[14,15] The activation energy (E_a = 14.6 kJ/mol) has been reported in the formation of copper vacancies in $Cu_{2-x}S$ nanodisks oxidized by ambient oxygen.[16] Such a low E_a makes the LSPR band difficult to be fixed in copper chalcogenide NC systems. Several groups had reported how each factor, for example, size, shape or composition of the NCs, influenced the plasmonic properties individually.[13,14,16] However, these conclusions could not be integrated simply, because the influence factors were correlated with each other. Zou's group[17] had reported the plasmonic absorption peak of $Cu_{2-x}S$ NCs showed weak size dependence, which contradicted with the results reported by Alivisatos' group.[13] The mutable crystal structure and stoichiometry complicated the plasmonic properties of the copper chalcogenide NCs, due to the variability of the chemical synthesis and the polymorphic nature of the copper chalcogenide compounds.[16]

All above make it hard to systematically investigate the relationship between the LSPR properties and the geometry,

Received: May 30, 2015
Published: August 28, 2015

DOI: 10.1021/jacs.5b05591
J. Am. Chem. Soc. 2015, 137, 12006−12012

composition, and dielectric environment in copper chalcogenide NCs. To accomplish this, two requirements should be met: (i) copper chalcogenide NCs should be synthesized controllably (including delicate tailoring of the size, composition, and encapsulation); (ii) the spectra of plasmonic bands should be collected under a relatively steady state. Various methods have been developed to fabricate the copper chalcogenide NCs for the study of their LSPR properties.[18−20] However, the size distributions of these NCs are relatively wide, rendering the accuracy and reproducibility of spectral characterizations unable to be guaranteed. Therefore, homogeneous copper chalcogenide NCs of high monodispersity are necessary in order to explore the structure−response relationship.[13] For the acquisition of the steady state, one can attempt to find a boundary value during the LSPR modulation via carrier concentration tuning; that is, the relationship can be investigated by tuning the plasmonic resonance absorption band to its limiting condition (denoted "pinning" phenomena of the plasmonic absorption). Experimentally, the pinning of LSPR band is recognized by the coincidence of the peak position of the last two absorption spectra after the tuning process.

In this report, we achieve the controllable synthesis of the well-monodisperse copper chalcogenide NCs by using Cu_3N nanoparticles as copper precursors through a facile one-pot method. The size of $Cu_{2-x}S$ NCs and the composition of the ternary $Cu_{2-x}S_ySe_{1-y}$ NCs can be tuned systematically by adjusting the copper and chalcogen precursor ratios. The UV−vis-NIR absorption analysis shows the pinning of LSPR absorption is relevant to the size and composition of the copper chalcogenide NCs. Furthermore, the $Cu_{2-x}S$ NCs are encapsulated by two graphene single-layers on a quartz substrate and the pinning phenomena of the sandwich-type structure showed a surrounding environment-related behavior.

EXPERIMENTAL SECTION

Materials. All chemicals have been used without further purification. Cupric nitrate ($Cu(NO_3)_2{\cdot}3H_2O$, A.R.) and ferric nitrate ($Fe(NO_3)_3{\cdot}9H_2O$, A.R.) were supplied by Xilong Chemicals Co. Ltd., China. Ammonium diethyldithiocarbamate and 1-hexadecylamine (HDA, 90%) were purchased from Sigma-Aldrich. 1-Octadecene (ODE, 90%), 1-dodecanethiol (DDT, 98%), diphenyl diselenide (98%), and cerium(IV) ammonium nitrate ($(NH_4)_2Ce(NO_3)_6$, 98+%) were obtained from Alfa Aesar. Tetrachloromethane (CCl_4, 99.9%), toluene (99.8%), and ethanol (99.9%) were supplied by Tianjin Kermel Chemical Reagent Co. Ltd., China.

Controllable Synthesis of Copper Chalcogenide Nanocrystals. The syntheses of copper chalcogenide NCs were performed under air-free conditions using a standard Schlenk-line technique.[21,22] In a typical synthesis, the Cu_3N nanoparticles were first synthesized as the copper precursor, following published procedures with slight modification.[23] To synthesize $Cu_{2-x}S$ NCs of 7.2 nm size, 8 mg (0.04 mmol) Cu_3N nanoparticles and 20 mg (0.12 mmol) of ammonium diethyldithiocarbamate as copper and sulfur precursor, respectively, were dissolved in 1-dodecanethiol (10 mL) and 1-octadecene (10 mL) mixed solvent at 60 °C. Then the blue solution was degassed at 100 °C for at least 30 min with the color becoming turbid white. The flask was then purged with argon and kept under an argon atmosphere during the whole reaction. The temperature was increased to 180 °C at a rate of ∼4 °C/min with the color changing from bright yellow to orange then to dark brown. After maintained at 180 °C for 30 min, the reaction mixture was cooled to ∼70 °C and centrifuged at 8000 rpm for 5 min. The NCs were washed three times with toluene/ethanol solvent and redispersed in tetrachloromethane (CCl_4) for optical characterization. To tune the size and composition, appropriate copper-to-sulfur and sulfur-to-selenium ratio was used, respectively, as detailed in the Supporting Information.

The growth process of the NCs was studied according to the previous report.[24] Aliquots (∼1 mL) of the reaction mixture were taken from the reaction flask at different reaction times and immediately precipitated in 3 mL methanol. The mass of aliquots was calculated by subtracting the mass of the methanol from the total mass of the mixture. The precipitate was isolated by centrifugation and washed with methanol and toluene several times. The sample was redispersed in toluene for TEM characterization. To determine the exact mass of the sample, the precipitates were dried under vacuum and digested by an HCl/HNO_3 (v/v = 3:1) solution for ICP measurements.

Fabrication of the Sandwich-like Heterostructure. To fabricate the sandwich-like heterostructure, single layer graphene (s-G) was first grown using a chemical vapor deposition process[25,26] and then transferred onto a quartz or Si-SiO_2 (300 nm SiO_2) substrate using polymethyl methacrylate (PMMA) as supporting material.[27,28] This was used as the bottom graphene layer. Then, the $Cu_{2-x}S$ NC solution (diluted, ∼30 μL) was dispensed on the s-G/Quartz or s-G/Si-SiO_2 substrate using a pipet. Through the coffee-ring effect, the NCs self-assembled on the substrate spontaneously. Finally, the top single layer graphene was immediately transferred to cover the $Cu_{2-x}S$ NCs.

Oxidation Tuning Methods. Metal salt solutions and atmospheric oxygen were used respectively to oxidize the $Cu_{2-x}S$ nanocrystals in order to tune the LSPR absorption peaks. First, the as-synthesized $Cu_{2-x}S$ NCs were dissolved in CCl_4 to form a stable and clear solution. For the metal salt oxidation method, the $Cu_{2-x}S$ NC solution were oxidized by adding 5 μL 0.1 M $Fe(NO_3)_3$ or $(NH_4)_2Ce(NO_3)_6$ ethanol solution per hour, and then the mixed solution was used to measure the extinction spectrum immediately after each addition. For the air oxidation, the $Cu_{2-x}S$ NC solution was kept in a vial filled with the ambient atmosphere.

Characterizations. The powder X-ray diffraction (PXRD) patterns of copper chalcogenide NCs were obtained on a Rigaku D/MAX-2000 diffractometer with Cu Kα radiation. Transmission electron microscopy (TEM) and high-resolution TEM (HRTEM) observations for particle morphology and structure were done using a Tecnai F20 TEM operated at 200 kV. Energy dispersive X-ray spectroscopy (EDX) analysis and bright field scanning transmission electron microscopy (BF-STEM) were performed on a FEG-TEM (JEM-2100F, JEOL) operated at 200 kV. The high-resolution mass spectrum (HRMS) was obtained by a Fourier transform mass spectrometer (Apex IV, Bruker). The copper concentration in the digested solution was determined by inductively coupled plasma-atomic emission spectrometer (ICP, Profile Spec, Leeman). Atomic force microscopy (AFM, Veeco NanoScope IIIA, Veeco Co.) was used to measure the thickness of the sandwich-type structure. Raman spectra were collected by a Horiba HR800 Raman system with 514.5 nm excitation and ∼1 × 1 μm^2 of the laser spot size. Optical absorption spectra of colloidal solutions and sandwich-type heterostructures were measured using a UV−vis-NIR spectrometer (Lambda 950, PerkinElmer or U-4100, Hitachi).

RESULTS AND DISCUSSION

Controllable Synthesis of Monodisperse Copper Chalcogenide Nanocrystals. The highly monodisperse copper chalcogenide NCs were synthesized through a facile one-pot route by using Cu_3N nanoparticles (Figure S1) as the copper precursor. Figure 1a−c showed the representative transmission electron microscopy (TEM) and high-resolution TEM (HRTEM) images of copper sulfide nanocrystals. The as-synthesized nanocrystals were nearly monodisperse with an average diameter of 7.1 ± 0.3 nm and, correspondingly, self-assembled into a two-dimensional (2D) array (Figure 1a and b). The HRTEM image of an individual nanocrystal showed distinct lattice fringes, indicating the NCs were well crystallized (Figure 1c). The calibrated lattice spacing (3.4 Å) can be

DOI: 10.1021/jacs.5b05591
J. Am. Chem. Soc. 2015, 137, 12006−12012

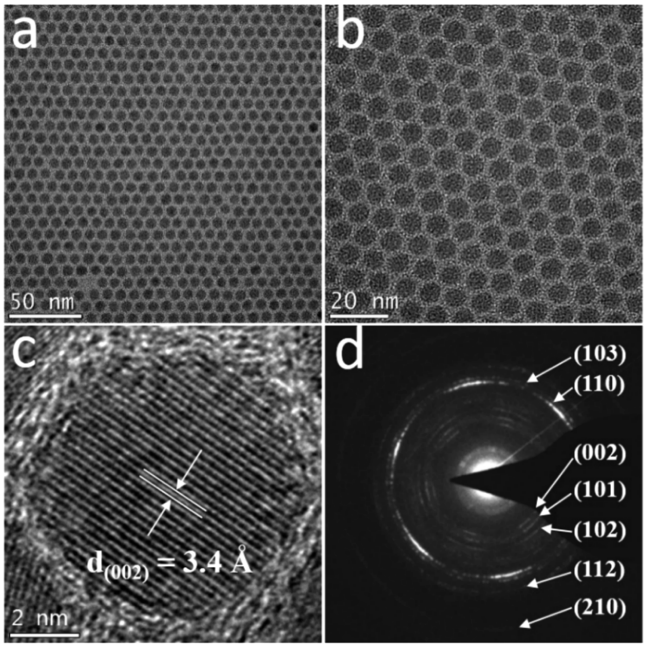

Figure 1. (a, b) Low- and high-magnification TEM images of monodisperse $Cu_{2-x}S$ nanocrystals. (c) High-resolution TEM image and (d) SAED pattern of as-synthesized $Cu_{2-x}S$ nanocrystals.

indexed to the (002) plane of hexagonal $Cu_{2-x}S$. Seven rings in the selected area electron diffraction (SAED) pattern (Figure 1d) were well consistent with the standard diffraction patterns of hexagonal Cu_2S structure (JCPDS 26-1116). It should be noted that each ring displayed six symmetrical arcs, which indicated that the nanocrystal building blocks of the 2D assembly had a preferential orientation.[29,30] The excellent monodispersity can be attributed to the homogeneous environment around the nanocrystal nuclei during the growth period, which is necessary for the focusing of size distribution.[31] The possible reaction mechanism was proposed as shown in Scheme 1.

Scheme 1. Proposed Formation Mechanism of Cu_2S Nanocrystals from Cu_3N Precursors

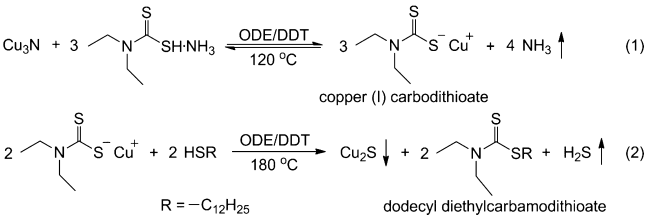

As the temperature increased to 120 °C, the Cu_3N precursors decomposed into copper(I) carbodithioate (reaction 1) and the solution color changed from brown to light yellow. When elevating the temperature to 180 °C, the copper(I) carbodithioate dissociated to form black brown Cu_2S nanocrystals capped with dodecanethiol (reaction 2). Meanwhile, there were considerable number of bubbles formed and released from the reaction solution at elevated temperatures, which may be attributed to the formation of hydrogen sulfide and ammonia gases as shown in Scheme 1. The byproduct (dodecyl diethylcarbamodithioate)[32] was confirmed by high-resolution mass spectrometry (HRMS, Figure S2). Throughout the whole synthesis, the byproducts of these reactions were mainly gaseous or uncharged organic molecules. It was well accepted that the introduction of inorganic anions in the synthesis process of NCs would degrade the stability of the colloidal system through the electrostatic interactions between the charged nanoparticles. This might cause the broadening of the size distribution of NCs. However, Cu_3N, as the "uncontaminated" precursor, would not remain foreign ions (e.g., nitrate and sulfate ions) during the formation and decomposition process of copper carbodithioate, compared with using $Cu(NO_3)_2$ and $CuSO_4$ as copper precursors. Therefore, the homogeneous coordination environment of the nuclei facilitated the focusing of size distribution during the growth period of NCs.

The size of $Cu_{2-x}S$ nanocrystals can be readily tuned by adjusting the copper-to-sulfur ratio of the precursors (Figure 2). When the amount of Cu_3N precursor was fixed, the diameter of $Cu_{2-x}S$ NCs decreased systematically as the copper-to-sulfur (Cu/S) precursor ratio increased (Figure S3a). However, the Cu/S stoichiometry of the as-synthesized NCs with different sizes were all close to 2:1, which indicated the initial composition of NCs synthesized via our strategy did not change with the Cu/S ratio of the precursors (Figure S3b). The size distributions of these samples were all extremely narrow with the largest size variation of 5.6%. The mechanism of the size evolution was investigated by TEM and ICP characterizations (Figure S4). With the increase of sulfur precursor concentrations, the number of nanocrystals (nuclei) formed in the initial nucleation stage did not increase much, which might be contributed to the gradual decomposition of the precursor molecules. Thus, the amount of sulfur component mainly influenced the growth stage of nanocrystals controlled by the diffusion mechanism.[33] The remaining monomer concentration was higher for the reactions with more sulfur precursors, corresponding to the faster NC growth rate. Therefore, the more sulfur precursor was added, the larger nanocrystals obtained.

Recently, ternary alloyed semiconductor nanomaterials have been designed to produce novel properties by inheriting characteristics from their binary parents.[22] In plasmonics, they may provide an effective way to tune the LSPR band of the semiconductor NCs. To our best knowledge, little work on the relationship between the LSPR absorption and the composition of the ternary alloyed copper sulfide selenide ($Cu_{2-x}S_ySe_{1-y}$) NCs has been done to date. In our synthetic protocol, $Cu_{2-x}S_ySe_{1-y}$ nanocrystals can be synthesized by adding diphenyl diselenide into the initial reactants. When the solution was heated, the sulfur and selenium precursor decomposed simultaneously and reacted with copper complex, resulting the formation of $Cu_{2-x}S_ySe_{1-y}$ NCs.[22] TEM image (Figure 3a) shows the ternary alloyed $Cu_{2-x}S_ySe_{1-y}$ NCs were nearly monodisperse with the size of 8.8 ± 0.6 nm. The fast Fourier transform (FFT) pattern (inset) indicated the as-synthesized $Cu_{2-x}S_ySe_{1-y}$ NCs formed the hexagonal 2D superlattice. Figure 3c shows the X-ray diffraction (XRD) patterns of the as-synthesized copper chalcogenide NCs with different composition ratios. Curves 1−3 show that all the samples had a hexagonal structure (Cu_2S, JCPDS 21-1116; space group 194, $P6_3/mmc$) with slightly different lattice parameters. The magnified (103) peaks (Figure 3d) shifted to small diffraction angles with the increase of Se content. This was contributed to the larger atomic size of Se than S, resulting in the increased size of the crystallographic unit cell.[34] The two peaks (at 32°

DOI: 10.1021/jacs.5b05591
J. Am. Chem. Soc. 2015, 137, 12006−12012

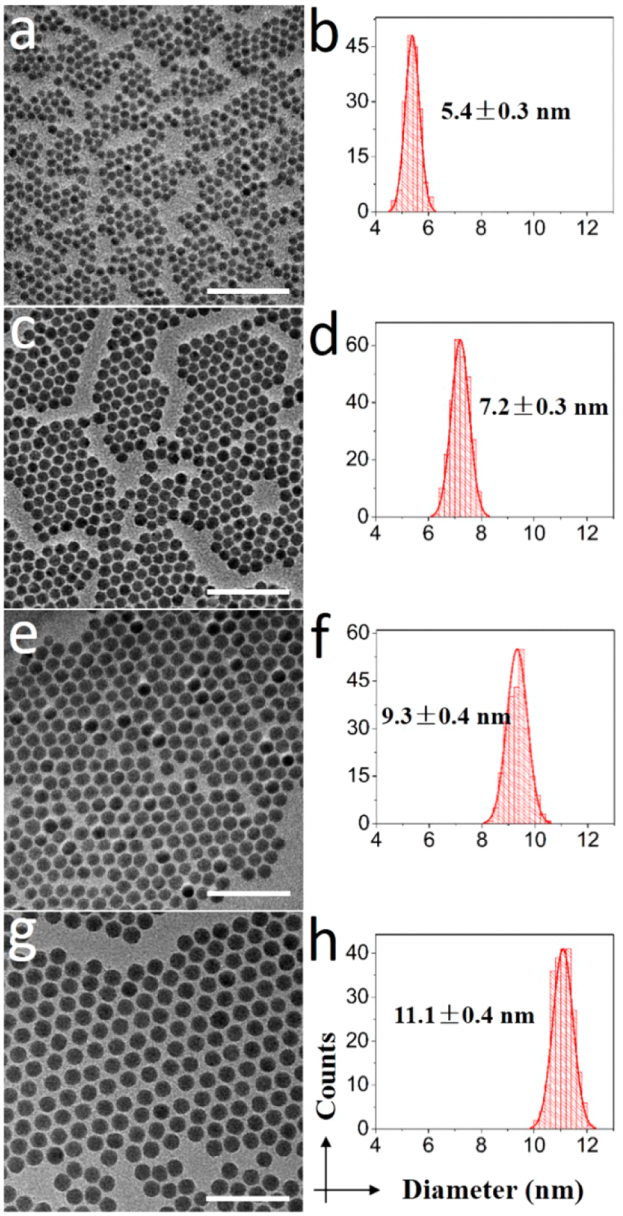

Figure 2. TEM images (left) and the corresponding size distribution histograms (right) of NC samples with average size of (a, b) 5.4 ± 0.3 nm, (c, d) 7.2 ± 0.3 nm, (e, f) 9.3 ± 0.4 nm, and (g, h) 11.1 ± 0.4 nm. The Cu/S ratio of the precursors equals 2.0, 1.0, 0.5, and 0.3, respectively. All the images with the same scale bar = 50 nm.

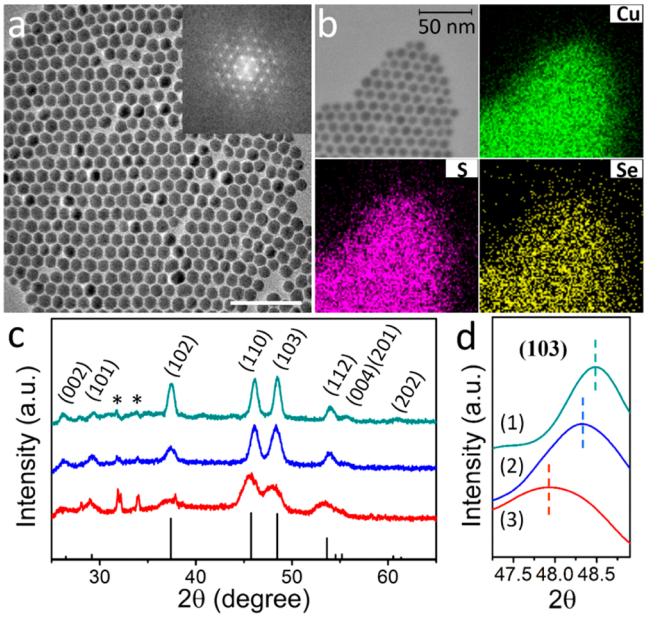

Figure 3. (a) TEM image of $Cu_{2-x}S_ySe_{1-y}$ NCs with the inset showing the fast Fourier transform (FFT) pattern (scale bar = 50 nm). (b) TEM bright field image and Cu, S, Se element mapping of $Cu_{2-x}S_ySe_{1-y}$ nanocrystals. (c, d) XRD spectra of samples with different Cu/S/Se ratios: (1) 64:36:0, (2) 64:32:4, and (3) 65:12:23. The drop lines show the standard pattern of chalcocite (JCPDS 26-1116), and the asterisks mark the peaks of djurleite (JCPDS 34-660).

and 34°) marked by asterisks could possibly be assigned to the djurleite phase ($Cu_{31}S_{16}$, JCPDS 34-660) of copper chalcogenide NCs. There were no obvious peaks of copper selenide phases in XRD patterns, indicating the homogeneous fusion of the three elements within the NCs. Combining the elemental mapping (Figure 3b) with the XRD evidence above, we confirmed that Cu, S, and Se elements were uniformly distributed among the nanocrystals. The Cu:S:Se ratios were determined by the energy-dispersive X-ray spectroscopy (EDX) as shown in Figure S5. When the ratios of the initial chalcogen amount (Se/S) was controlled to be 1:2, 1:1, and 2:1, the final copper chalcogenide NCs were characterized as $Cu_{61}S_{37}Se_2$, $Cu_{64}S_{29}Se_7$, and $Cu_{65}S_{12}Se_{23}$, respectively. Thus, the composition of monodispersed ternary alloyed $Cu_{2-x}S_ySe_{1-y}$ NCs can be controlled by tuning the ratio of S and Se precursors in the Cu_3N-precursor protocol.

Oxidization Tuning and Pinning of Plasmonic Absorption in Copper Chalcogenide Nanocrystal Systems. Three different methods had been performed to oxidize the $Cu_{2-x}S$ colloids to tune the LSPR absorptions. Compared with Fe^{3+} and Ce^{4+} ions in ethanol solution, the dissolved oxygen in CCl_4 had been proved to be a clean and moderate oxidant for the Cu^+ to Cu^{2+} reaction (Figure S6). Therefore, the oxidation tuning experiments in this work were achieved by means of the dissolved oxygen. As the oxidation process evolved, the LSPR bands of all the NCs with different sizes moved from lower energy to higher energy, along with the resonant absorption intensities increasing gradually (Figure 4). However, the bandgap absorption in UV and visible range had little shift in contrast to the NIR plasmonic absorption. The pinning of the LSPR band were obtained by oxidation via ambient oxygen for several thousands of hours. The resonance absorption correlates with the excess free carrier density in the NCs and can be describe by the Drude model.[8,9] Under the resonance condition, we can deduce the LSPR frequency ω_{sp} expressed as

$$\omega_{sp} = \sqrt{\frac{\omega_p^2}{1 + 2\varepsilon_m} - \gamma^2} \quad (1)$$

where ω_p is the bulk plasma oscillation frequency, ε_m is the dielectric constant of the surrounding medium, and γ is the damping parameter, which numerically equals to the full width at half-maximum (fwhm) of the plasmon resonance band. For the 9.2 ± 0.4 nm NCs oxidized for 2650 h (Figure 4b), the plasmonic absorption spectra showed the resonance energy ω_{sp} is 1.17 eV and the fwhm is 0.75 eV. Thus, we can estimate the bulk plasma frequency ω_p of the free carriers in copper sulfide

DOI: 10.1021/jacs.5b05591
J. Am. Chem. Soc. 2015, 137, 12006−12012

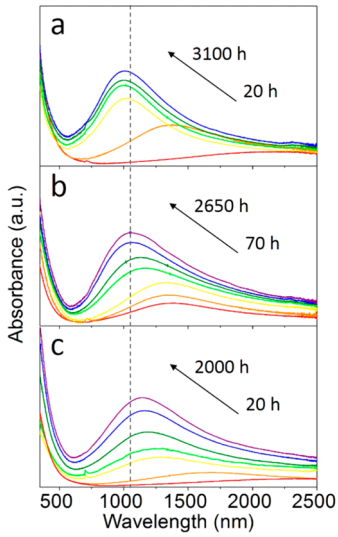

Figure 4. Evolution and pinning of LSPR absorption spectra of the $Cu_{2-x}S$ NCs with different diameters: (a) 11.0 ± 0.3 nm, (b) 9.2 ± 0.4 nm, and (c) 5.4 ± 0.3 nm. The spectra were collected after oxidized by the dissolved oxygen in CCl_4 for different times: (a) 20, 70, 1000, 1500, 2800, 3100 h; (b) 70, 100, 130, 750, 1050, 2350, 2650 h; (c) 20, 70, 550, 850, 1400, 1700, 2000 h. All of the samples showed the pinning state of LSPR band based on the peak position of the last two spectra.

to be 3.25 eV, ignoring the ligand shell effects and regarding the external medium as solely tetrachloromethane ($\varepsilon_m = 2.24$). The bulk plasma frequency is related to the dopant density by the formula:

$$\omega_p^2 = \frac{N_h e^2}{\varepsilon_0 m^*} \quad (2)$$

where N_h is hole carrier concentration, ε_0 is free space permittivity, and m^* is hole effective mass estimated as $0.8m_0$, where m_0 is the electron mass. Based on these calculations, we are able to estimate the critical value of N_h to be 2.9×10^{21} cm^{-3}. Regarding the nanocrystals as spheres with the diameter of 9.2 nm, we estimate ~1190 free holes per nanocrystal under the pinning conditions.

Figure 4 shows the pinning positions of the LSPR absorption peaks of $Cu_{2-x}S$ NCs were 1140, 1060, and 1005 nm for the ones with diameters of 5.4 ± 0.3, 9.2 ± 0.4, and 11.0 ± 0.3 nm, respectively. The pinning position was observed to blue-shift with decreasing nanocrystal size, also called the size-dependent property, which can be qualitatively explained by the Drude model. In the case of nanocrystals whose size D is comparable to the mean free path of the carriers, the plasmonic frequency in small nanocrystals is demonstrated as

$$\omega_{sp} = \sqrt{\frac{\omega_p^2}{1 + 2\varepsilon_m} - \left(\gamma_b + A\frac{\upsilon_F}{D}\right)^2} \quad (3)$$

where γ_b is the damping parameter in the bulk, ν_F is the Fermi velocity of the nanocrystal and A is an empirical constant. Under the pinning condition, the $Cu_{2-x}S$ NCs with different sizes had the same copper vacancy density, crystalline phase, and similar chemical interface, except the diameter of the nanocrystals. After the long-term oxidation tuning process, the $Cu_{2-x}S$ nanocrystals underwent a size decreasing process (Figure S7) with size decreased from 5.4 ± 0.3, 9.2 ± 0.4, and 11.0 ± 0.3 nm to 5.3 ± 0.4, 8.5 ± 0.8, and 9.8 ± 0.5 nm, respectively. In spite of the existence of the digestive ripening,[17] the order of particle sizes did not change. Therefore, with the size of NCs increasing, the damping parameter γ (effective collision frequency) decreased, resulting in the increment of ω_{sp}.[13] Our results demonstrated that the size-dependent plasmonic property of copper chalcogenide NCs was distinguishable under the pinning state, which was inconsistent with the previous report.[17]

Figure 5a displays the pinning absorption spectra of $Cu_{2-x}S_ySe_{1-y}$ NCs in CCl_4 after more than 1500 h oxidation.

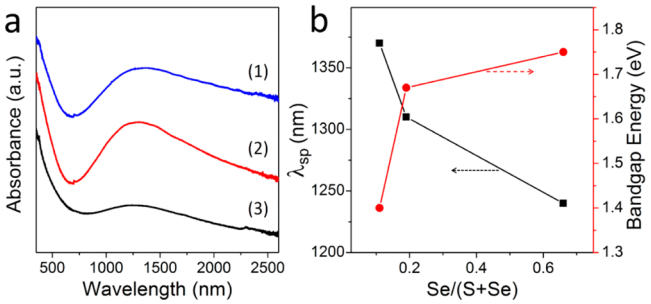

Figure 5. (a) Pinning spectra of LSPR absorption of $Cu_{2-x}S_ySe_{1-y}$ NCs: (1) $Cu_{1.96}S_{0.89}Se_{0.11}$, (2) $Cu_{1.96}S_{0.81}Se_{0.19}$, and (3) $Cu_{1.97}S_{0.34}Se_{0.66}$. (b) Plasmonic resonance pinning frequency and bandgap energy of $Cu_{2-x}S_ySe_{1-y}$ NCs with different chalcogen compositions.

The physical parameters of these NCs were estimated and listed in Table 1. According to the size-dependent effect demonstrated above, we controlled the synthesis of samples in Figure 5a with similar diameters ~9 nm (Figure S8) to exclude the influence of size. Figure 5b showed the $Cu_{2-x}S_ySe_{1-y}$ NC had the larger bandgap energy with the larger Se content, which was consistent with the previous results.[22] However, it showed the negative correlation between the LSPR pinning wavelength λ_{sp} and the Se content in the $Cu_{2-x}S_ySe_{1-y}$ NCs. This relationship can be explained by the changes in effective mass of free carriers of the NCs with different amount of doping Se element. For Cu_2Se, the effective mass $m^* = 0.2-0.25m_0$ with the free hole concentration > 10^{21} cm^{-3}.[35,36] While it is $0.8m_0$ for $Cu_{2-x}S$ NCs, we can safely estimate the m^* of $Cu_{2-x}S_ySe_{1-y}$ NCs decreases with the increase of Se content. From eqs 1 and 2, the plasmonic pinning frequency is expressed as

$$\omega_{sp} = \sqrt{\frac{N_h e^2}{\varepsilon_0 m(1 + 2\varepsilon_m)} - \gamma^2} \quad (4)$$

This formula gives us a qualitative explanation on the positive relationship between ω_{sp} and Se/(S + Se) ratio, that is, the

Table 1. Parameters of $Cu_{2-x}S_ySe_{1-y}$ NCs for the Plasmonic Pinning Measurement

Se/(S + Se)	diameter, nm	band gap energy, eV[a]	oxidation time, h	pinning wavelength, nm
0.11	9.6 ± 1.3	1.40	1560	1370
0.19	8.8 ± 0.6	1.67	1560	1310
0.66	9.0 ± 0.7	1.75	1590	1240

[a]The band gap energy was obtained based on the relation of $(\alpha h\upsilon)^{1/2}$ versus $h\upsilon$, where α, h, and υ represented the absorbance, Planck's constant, and frequency, respectively. Detailed in Figure S9 in the Supporting Information.

DOI: 10.1021/jacs.5b05591
J. Am. Chem. Soc. 2015, 137, 12006−12012

higher Se content, the lower effective mass of free holes, then the higher plasmonic pinning frequency.

Encapsulation of $Cu_{2-x}S$ NCs by Single-Layer Graphene and the Plasmonic Absorption Properties. To investigate the effect of dielectric environment on the LSPR absorption, we encapsulated the as-prepared $Cu_{2-x}S$ NCs by two layers of single-layer graphene on the quartz substrate and compared the plasmonic absorption of the sandwich-style structure with that of the counterparts dissolved in nonpolar solvent. The structure was fabricated by sequential transfer of bottom graphene, deposition of $Cu_{2-x}S$ NCs and coverage of top graphene (Figure 6a). Raman Spectroscopy analysis (Figure S10) was introduced to confirm the successful fabrication of the s-G/$Cu_{2-x}S$ NCs/s-G sandwich-type structures, with the G to 2D intensity ratio proved the single-layer nature of graphene.[37−39] AFM image (Figure 6a) showed the multilayer nature (several to more than a dozen layers) of the $Cu_{2-x}S$ NCs (11.0 ± 0.3 nm) encapsulated by the two layers of s-G. The $Cu_{2-x}S$ NCs in the sandwich-type structures (curve 1) showed a blue shift of λ_{sp} from 1650 to 1570 nm (Figure 6b) compared with the counterpart dissolved in CCl_4 (curve 2). According to the previous report on copper sulfide nanodisks,[40] the dipole−dipole coupling for samples with high Cu content was quite weak (λ_{sp} shift of ∼1%) both for the in-plane and out-of-plane mode. Therefore, the relatively large shift (∼5%) of λ_{sp} was dominated by the difference of dielectric environment, which could be explained by eq 1. In the sandwich-type structure, the dielectric constant of the environment of $Cu_{2-x}S$ NCs (ε = 2.0) was obtained from the standard approximation, $\varepsilon = (\varepsilon_G + \varepsilon_{Q/G})/2$, where the dielectric constant of the top-layer graphene ε_G = 2.2 was extracted from the experimental value for the suspended graphene, and $\varepsilon_{Q/G}$ = 1.8 for graphene on the quartz substrate.[41−43] This value was smaller than the one of $Cu_{2-x}S$ NCs surrounding by CCl_4 (ε = 2.24). Therefore, the decrease of ε_m accounts for the blue shift of the plasmonic band in the Q/s-G/$Cu_{2-x}S$ NCs/s-G sandwich-type structures. Figure 6b,c shows the evolution of the LSPR absorption in these structures oxidized by the ambient oxygen. The $Cu_{2-x}S$ NCs with different initial oxidation states (line 1−4, Figure 6c) showed different oxidation speeds; that is, the sample with larger initial λ_{sp} exhibited faster oxidation speed due to the higher reduction potential. The $Cu_{2-x}S$ NCs without the coverage of the top layer graphene (black line) showed a continuous oxidation along with the peak wavelength blue-shifting to ∼1360 nm after 130 days and no pinning was observed. However, the encapsulated samples showed the plasmonic absorption pinning at 1525−1550 nm no matter what initial oxidation states they were. The pinning wavelengths were longer than those of $Cu_{2-x}S$ NCs in CCl_4 solution, because of the lower carrier concentration. If they had the same free carrier concentrations, the plasmonic absorption pinning peaks should exhibit blue shifts toward $Cu_{2-x}S$ NCs in CCl_4 solution as discussed above. Therefore, the encapsulation by two layers of graphene on quartz substrate not only changed the dielectric constant of the environment, but also changed the redox potential of the surrounding medium. The detailed reason would be further investigated in future research.

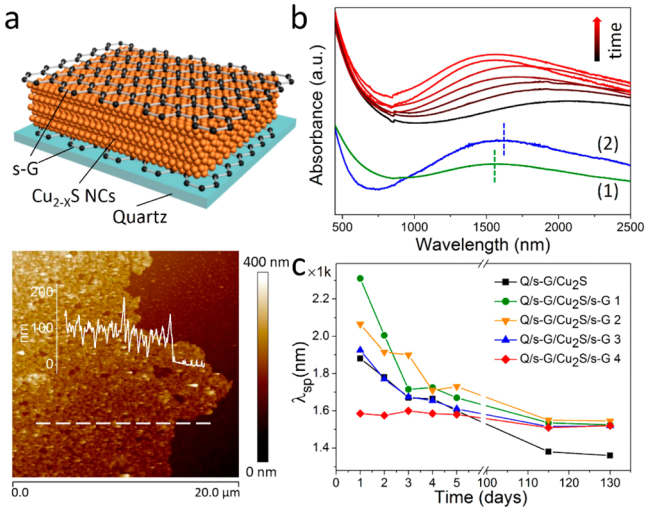

Figure 6. (a) Schematic depiction (upper panel) of single-layer graphene/$Cu_{2-x}S$ NCs/single-layer graphene (s-G/$Cu_{2-x}S$ NCs/s-G) sandwich-type structures on quartz substrate. A typical AFM image (lower panel) shows the thickness of the sandwich-type structure made by $Cu_{2-x}S$ NCs with size of 11.0 ± 0.3 nm. (b) UV−vis-NIR absorption of $Cu_{2-x}S$ NCs in CCl_4 and in the sandwich-type structure (lower panel) and the absorption evolution of the encapsulated $Cu_{2-x}S$ NCs by graphene (upper panel). (c) Evolutions of LSPR absorption pinning wavelength in graphene-encapsulated $Cu_{2-x}S$ NC structures with different initial oxidation states.

CONCLUSIONS

In this work, we have presented a one-pot strategy to prepare copper chalcogenide NCs of high monodispersity by using Cu_3N nanoparticles as the "uncontaminated" copper precursors. The size and composition can be controlled by the copper-to-sulfur ratio and selenium content, respectively. The pinning phenomena of plasmonic resonance absorption are investigated in the well-tailored system. The pinning frequency is positively related to the size of $Cu_{2-x}S$ NCs and the selenium content of $Cu_{2-x}S_ySe_{1-y}$ NCs, which can be explained by introducing the surface scattering and effective mass of free carriers. By encapsulating the $Cu_{2-x}S$ NCs with graphene, the dielectric environment can be tuned, whereas the plasmonic pinning position is also associated with the redox potential of the surrounding environment. These fundamental investigations on the relationship between plasmonic properties and the influence factors provide a systematic understanding of the LSPR absorption in the doped semiconductor NCs.

From the perspective of application, the high monodisperse copper chalcogenide NCs with uniform and accurate plasmonic absorption peaks (pinning state) are expected to exhibit the highest photothermal conversion efficiency compared with the polydisperse ones, which would furthest reduce the requirement on the power of exciting laser. It is of high significance to protect the normal cells from ablation by the exciting laser in the treatment of photothermal therapy. Furthermore, the monodisperse NCs with tunable size, composition and environment provide the potential to improve the spatial resolution of plasmonic-related techniques, such as promoting photothermal therapy and photoacoustic tomography to be applied on a nanometric biomolecule level.

ASSOCIATED CONTENT

Supporting Information

The Supporting Information is available free of charge on the ACS Publications website at DOI: 10.1021/jacs.5b05591.

Additional analytical data, spectra, and images (PDF)

DOI: 10.1021/jacs.5b05591
J. Am. Chem. Soc. 2015, 137, 12006−12012

AUTHOR INFORMATION

Corresponding Authors

*dsxu@pku.edu.cn

*liqi2010@pku.edu.cn

Notes

The authors declare no competing financial interest.

ACKNOWLEDGMENTS

This work was financially supported by the National Natural Science Foundation of China (Grant Nos. 21133001 and 21303004) and the National Key Basic Research Program of China (Grant Nos. 2011CB808702, 2013CB932601, and 2014CB239303).

REFERENCES

(1) Kelly, K. L.; Coronado, E.; Zhao, L. L.; Schatz, G. C. *J. Phys. Chem. B* **2003**, *107*, 668.

(2) Rycenga, M.; Cobley, C. M.; Zeng, J.; Li, W.; Moran, C. H.; Zhang, Q.; Qin, D.; Xia, Y. *Chem. Rev.* **2011**, *111*, 3669.

(3) Huang, X.; El-Sayed, I. H.; Qian, W.; El-Sayed, M. A. *J. Am. Chem. Soc.* **2006**, *128*, 2115.

(4) Moon, G. D.; Choi, S. W.; Cai, X.; Li, W.; Cho, E. C.; Jeong, U.; Wang, L. V.; Xia, Y. *J. Am. Chem. Soc.* **2011**, *133*, 4762.

(5) Mayer, K. M.; Hafner, J. H. *Chem. Rev.* **2011**, *111*, 3828.

(6) Linic, S.; Christopher, P.; Ingram, D. B. *Nat. Mater.* **2011**, *10*, 911.

(7) Lee, D. H.; Kwon, J. Y.; Maldonado, S.; Tuteja, A.; Boukai, A. *Nano Lett.* **2014**, *14*, 1961.

(8) Naik, G. V.; Shalaev, V. M.; Boltasseva, A. *Adv. Mater.* **2013**, *25*, 3264.

(9) Comin, A.; Manna, L. *Chem. Soc. Rev.* **2014**, *43*, 3957.

(10) Kovalenko, M. V.; Manna, L.; Cabot, A.; Hens, Z.; Talapin, D. V.; Kagan, C. R.; Klimov, V. I.; Rogach, A. L.; Reiss, P.; Milliron, D. J.; Guyot-Sionnnest, P.; Konstantatos, G.; Parak, W. J.; Hyeon, T.; Korgel, B. A.; Murray, C. B.; Heiss, W. *ACS Nano* **2015**, *9*, 1012.

(11) Martinson, A. B. F.; Riha, S. C.; Thimsen, E.; Elam, J. W.; Pellin, M. J. *Energy Environ. Sci.* **2013**, *6*, 1868.

(12) Bekenstein, Y.; Vinokurov, K.; Keren-Zur, S.; Hadar, I.; Schilt, Y.; Raviv, U.; Millo, O.; Banin, U. *Nano Lett.* **2014**, *14*, 1349.

(13) Luther, J. M.; Jain, P. K.; Ewers, T.; Alivisatos, A. P. *Nat. Mater.* **2011**, *10*, 361.

(14) Saldanha, P. L.; Brescia, R.; Prato, M.; Li, H.; Povia, M.; Manna, L.; Lesnyak, V. *Chem. Mater.* **2014**, *26*, 1442.

(15) Dorfs, D.; Härtling, T.; Miszta, K.; Bigall, N. C.; Kim, M. R.; Genovese, A.; Falqui, A.; Povia, M.; Manna, L. *J. Am. Chem. Soc.* **2011**, *133*, 11175.

(16) Hsu, S.-W.; Bryks, W.; Tao, A. R. *Chem. Mater.* **2012**, *24*, 3765.

(17) Liu, L. G.; Zhong, H. Z.; Bai, Z. L.; Zhang, T.; Fu, W. P.; Shi, L. J.; Xie, H. Y.; Deng, L. G.; Zou, B. S. *Chem. Mater.* **2013**, *25*, 4828.

(18) Liu, X.; Wang, X. L.; Zhou, B.; Law, W.-C.; Cartwright, A. N.; Swihart, M. T. *Adv. Funct. Mater.* **2013**, *23*, 1256.

(19) Zhao, Y. X.; Pan, H. C.; Lou, Y. B.; Qiu, X. F.; Zhu, J. J.; Burda, C. *J. Am. Chem. Soc.* **2009**, *131*, 4253.

(20) Hsu, S.-W.; On, K.; Tao, A. R. *J. Am. Chem. Soc.* **2011**, *133*, 19072.

(21) Wu, Y.; Wadia, C.; Ma, W. L.; Sadtler, B.; Alivisatos, A. P. *Nano Lett.* **2008**, *8*, 2551.

(22) Wang, J. J.; Xue, D. J.; Guo, Y. G.; Hu, J. S.; Wan, L. J. *J. Am. Chem. Soc.* **2011**, *133*, 18558.

(23) Wu, H. B.; Chen, W. *J. Am. Chem. Soc.* **2011**, *133*, 15236.

(24) Peng, Z. A.; Peng, X. G. *J. Am. Chem. Soc.* **2001**, *123*, 1389.

(25) Li, X.; Cai, W.; An, J.; Kim, S.; Nah, J.; Yang, D.; Piner, R.; Velamakanni, A.; Jung, I.; Tutuc, E.; Banerjee, S. K.; Colombo, L.; Ruoff, R. S. *Science* **2009**, *324*, 1312.

(26) Liu, L. X.; Zhou, H. L.; Cheng, R.; Chen, Y.; Lin, Y. C.; Qu, Y. Q.; Bai, J. W.; Ivanov, I. A.; Liu, G.; Huang, Y.; Duan, X. F. *J. Mater. Chem.* **2012**, *22*, 1498.

(27) Reina, A.; Son, H.; Jiao, L.; Fan, B.; Dresselhaus, M. S.; Liu, Z.; Kong, J. *J. Phys. Chem. C* **2008**, *112*, 17741.

(28) Kim, K. S.; Zhao, Y.; Jang, H.; Lee, S. Y.; Kim, J. M.; Kim, K. S.; Ahn, J.-H.; Kim, P.; Choi, J.-Y.; Hong, B. H. *Nature* **2009**, *457*, 706.

(29) Zhuang, Z. B.; Peng, Q.; Zhang, B.; Li, Y. D. *J. Am. Chem. Soc.* **2008**, *130*, 10482.

(30) Tang, Z. Y.; Kotov, N. A.; Giersig, M. *Science* **2002**, *297*, 237.

(31) Yin, Y. D.; Alivisatos, A. P. *Nature* **2005**, *437*, 664−670.

(32) The byproduct (dodecyl diethylcarbamodithioate) was detected by ESI-MS: $C_{17}H_{35}NS_2$ ($M + Na^+$) calculated 340.2109, found 340.1696.

(33) Kruszynska, M.; Borchert, H.; Bachmatiuk, A.; Rümmeli, M. H.; Büchner, B.; Parisi, J.; Kolny-Olesiak, J. *ACS Nano* **2012**, *6*, 5889.

(34) Xu, J.; Tang, Y. B.; Chen, X.; Luan, C. Y.; Zhang, W. F.; Zapien, J. A.; Zhang, W. J.; Kwong, H.-L.; Meng, X. M.; Lee, S.-T.; Lee, C.-S. *Adv. Funct. Mater.* **2010**, *20*, 4190.

(35) Gorbachev, V. V.; Putilin, I. M. *Phys. Status Solidi A* **1973**, *16*, 553.

(36) Mendelsberg, R. J.; Garcia, G.; Li, H. B.; Manna, L.; Milliron, D. J. *J. Phys. Chem. C* **2012**, *116*, 12226.

(37) Reina, A.; Jia, X. T.; Ho, J.; Nezich, D.; Son, H. B.; Bulovic, V.; Dresselhaus, M. S.; Kong, J. *Nano Lett.* **2009**, *9*, 30.

(38) Ferrari, A. C.; Meyer, J. C.; Scardaci, V.; Casiraghi, C.; Lazzeri, M.; Mauri, F.; Piscanec, S.; Jiang, D.; Novoselov, K. S.; Roth, S.; Geim, A. K. *Phys. Rev. Lett.* **2006**, *97*, 187401.

(39) Das, A.; Pisana, S.; Chakraborty, B.; Piscanec, S.; Saha, S. K.; Waghmare, U. V.; Novoselov, K. S.; Krishnamurthy, H. R.; Geim, A. K.; Ferrari, A. C.; Sood, A. K. *Nat. Nanotechnol.* **2008**, *3*, 210.

(40) Hsu, S.-W.; Ngo, C.; Tao, A. R. *Nano Lett.* **2014**, *14*, 2372.

(41) Hwang, C.; Siegel, D. A.; Mo, S. K.; Regan, W.; Ismach, A.; Zhang, Y. G.; Zettl, A.; Lanzara, A. *Sci. Rep.* **2012**, *2*, 590.

(42) Bostwick, A.; Speck, F.; Seyller, T.; Horn, K.; Polini, M.; Asgari, R.; MacDonald, A. H.; Rotenberg, E. *Science* **2010**, *328*, 999.

(43) Elias, D. C.; Gorbachev, R. V.; Mayorov, A. S.; Morozov, S. V.; Zhukov, A. A.; Blake, P.; Ponomarenko, L. A.; Grigorieva, I. V.; Novoselov, K. S.; Guinea, F.; Geim, A. K. *Nat. Phys.* **2011**, *7*, 701.

DOI: 10.1021/jacs.5b05591
J. Am. Chem. Soc. 2015, 137, 12006−12012